Rapid Communications

Compression of liquid Ni and Co under extreme conditions explored by x-ray absorption spectroscopy

Silvia Boccato,[1,*] Raffaella Torchio,[1] Paola D'Angelo,[2] Angela Trapananti,[3] Innokenty Kantor,[1,†] Vanina Recoules,[4] Simone Anzellini,[5] Guillaume Morard,[6,‡] Tetsuo Irifune,[7] and Sakura Pascarelli[1]

[1]*European Synchrotron Radiation Facility (ESRF), Grenoble, France*

[2]*Department of Chemistry, University of Rome "La Sapienza," Rome, Italy*

[3]*School of Science and Technology, Physics Division, University of Camerino, Camerino, Italy*

[4]*CEA-DAM-DIF, F-91297 Arpajon, France*

[5]*Diamond Light Source Ltd., Harwell Science and Innovation Campus, Didcot, OX11 0DE, United Kingdom*

[6]*Institut de Minéralogie, de Physique des Matériaux, et de Cosmochimie (IMPMC), Sorbonne Université, UMR CNRS 7590, Muséum National d'Histoire Naturelle, UMR 206, F-75005, Paris, France*

[7]*Ehime University, Matsuyama, Japan*

(Received 22 January 2019; revised manuscript received 5 August 2019; published 8 November 2019)

The compression of liquid nickel and cobalt has been investigated up to 102 and 83 GPa, respectively, by x-ray absorption spectroscopy at the Ni and Co *K* edges, using laser-heated diamond anvil cell. A shortening of about 8%–10% of the metal bond distances is observed in the pressure range considered and the experimental results are confirmed by theoretical calculations. *Ab initio* quantum molecular dynamics calculations have been performed, providing a model pair distribution function for cobalt, used as a starting model in the extended x-ray absorption fine structure analysis. The specific volume of the liquid has also been estimated and compared to calculations in the literature. This work sets the basis for x-ray absorption spectroscopy studies of liquid metals under extreme conditions with potentially important implications for the understanding of Earth and planetary interiors.

DOI: 10.1103/PhysRevB.100.180101

Structural analysis of liquids at high pressure and temperature became possible with the appearance of third-generation synchrotrons [1]. In the last 20 years, a lot of experimental and theoretical efforts have been focused on the evaluation of the equation of state of liquids on iron and iron alloyed with light elements [2–12], with important implications in geophysics and material science. Despite this, the knowledge of the structure of liquid Fe as well as of the other 3*d* metals at high pressure (pair distribution function, first neighbor distance, coordination number, density) remains, from the experimental point of view, quite limited in terms of pressure range or information extracted. This is certainly not due to the lack of interest in the topic, but rather to the challenging experimental conditions which have only recently started to be surmounted, allowing one to obtain first reliable melting curves ([13–21], and references therein) and first structural information on the melts. Nickel and cobalt are 3*d* metals and due to their vicinity in the periodic table, their structural and magnetic behavior has often been compared to iron [22–24]. Computational studies on the local structure of liquid nickel [25,26] and cobalt [19,27] at high pressure exist, while to the best of our knowledge an experimental investigation of the structure of these melts under pressure is still missing. The only studies presented in the literature on pure liquid nickel and cobalt deal with the structure and properties of the material at ambient pressure [28–35].

In this work we report the experimental structural characterization of liquid nickel and cobalt at high pressure (up to 102 and 83 GPa, respectively) by x-ray absorption spectroscopy (XAS) technique. By analyzing the extended x-ray absorption fine structure (EXAFS) region of the absorption spectra it was possible to quantitatively determine the compression of liquid nickel and cobalt. In a XAS experiment the absorption coefficient is measured as a function of the photon energy for a selected element (photoabsorber). The effect of the surrounding atoms is to produce interferences observable as oscillations in the cross-section signal. The analysis of the oscillating signal provides an accurate determination of the first neighbor coordination distances around the photoabsorber. This makes XAS a suitable structural probe for systems characterized by short-range order, such as disordered or liquid substances.

High pressure and temperature conditions were produced in laser-heated diamond anvil cell. *In situ* XAS experiments were carried out at the ID24 beamline of the European Synchrotron Radiation Facility (ESRF) [36]. The samples, a 4-μm-thick polycrystalline nickel foil 99.95% (Goodfellow) and a 4-μm-thick cobalt deposition (Eric Monsifrot, SARL

*Present address: Institut de Minéralogie, de Physique des Matériaux, et de Cosmochimie (IMPMC), Sorbonne Université, UMR CNRS 7590, Muséum National d'Histoire Naturelle, UMR 206, F-75005 Paris, France; silvia.boccato@upmc.

†Present address: Department of Physics, Technical University of Denmark, Kgs. Lyngby, Denmark.

‡Present address: ISTerre, Université Grenoble Alpes, Grenoble, France.

DEPHIS, Etupes, France), were loaded into the diamond anvil cell sample chambers with diameters variable between 70 and 120 μm. The holes were drilled in 30-μm-thick rhenium gaskets. The samples were insulated from the diamonds by two KCl disks previously dried at 120 °C for at least 4 h. The diamonds were nanopolycrystalline to avoid glitches in the XAS signal produced by single-crystal Bragg reflections [37]. The pressure was measured using the ruby ($Cr:Al_2O_3$) fluorescence signal [38] and its error was evaluated as about 10% of the measured pressure. Thermal pressure correction was applied to the data as explained in Refs. [18,20]. After careful alignment of x rays, infrared lasers, and temperature measurement optical path, the temperature was varied by changing the power of two lasers. The temperature error bar was determined as the standard deviation of the two colors fit [39,40]. The measurement strategy, with details on the alignment procedure, temperature metrology, and possible sources of systematic errors are detailed in the Supplemental Material [41] as well as in Refs. [16,20,40,42]. A description of the laser heating system used, coupled with the ID24 beamline at the ESRF, is detailed in Refs. [43,44]. A polychromatic x-ray beam covering an energy range between 8250 and 8610 eV for nickel, and between 7640 and 8055 eV for cobalt, was focused on the sample in order to obtain spot sizes of 6×7 μm^2 and 4×5 μm^2 (vertical $\times$ horizontal) full width at half maximum, respectively. XAS data were collected with a FreLoN camera [45] and the pixel-energy calibration was performed using either a nickel or a cobalt foil as standard. In each heating cycle, once the target pressure was reached, the laser power was gradually increased until the complete melting of the sample was observed. Each heating cycle was performed on a new portion of the sample to avoid contamination. Chemical reactions were monitored by comparing the XAS before and after heating, as in Ref. [20]. Nickel and cobalt are fcc crystals before melting [18,46]. The solid-liquid phase transition was identified by the loss of the edge shoulder and the flattening of the first two oscillations in the XAS spectrum (see Fig. 1). XAS melting criterion has already been used for several metals [15,16,33,47] (and references within) and its validation for nickel and cobalt was discussed in Refs. [20,42].

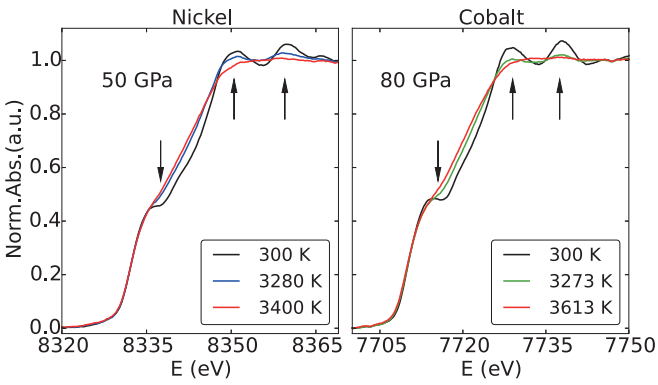

FIG. 1. K-edge XAS spectra of nickel and cobalt (left and right panels, respectively). The red spectra are associated with the first liquid sample while the blue and green ones are associated with the last high-temperature solid for nickel and cobalt, respectively. The black spectra are measured at ambient temperature. The validation of the melting criterion for these sets of data is provided in Refs. [20,42].

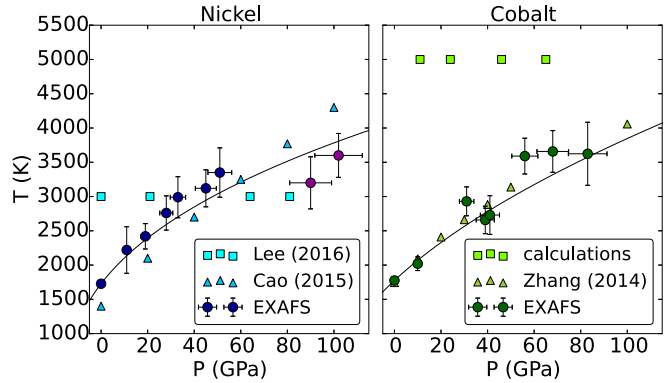

FIG. 2. Thermodynamic conditions of XAS data measurements for pure liquid nickel (left panel, blue points) and cobalt (right panel, green points) considered in this work for the analysis of first neighbors distances in the liquid. The purple circles in the left panel represent points where after melting a contamination with about 7% of NiO was detected. The thermodynamic conditions used in molecular dynamics simulations are also reported. Cyan triangles and squares refer to the values in Refs. [25,26] for nickel. Light-green squares refer to the thermodynamic conditions used for cobalt in the quantum molecular dynamics of this work, while green triangles refer to the values in Ref. [19]. The solid curves indicate the melting detected with XAS [20,42].

Complete melting is achieved when no further changes are detected in the x-ray absorption near-edge structure (XANES) upon increase of laser power. The pressure and temperature conditions of the K-edge XAS spectra of liquid nickel and cobalt analyzed in this work are illustrated in Fig. 2. The extended x-ray-absorption fine structure (EXAFS) experimental signals defined as the oscillation with respect to the atomic background cross section normalized to the corresponding K-edge channel cross section, are shown in the left and right panels of Fig. 3 for Ni and Co, respectively. The EXAFS spectra show the presence of a dominant, single frequency that is compatible with the detection of a single distance and this behavior is typical for very disordered systems. The EXAFS signals in Fig. 3 show a strong pressure dependence. In particular, there is a clear shift in the phase of the oscillations towards higher k values as pressure increases, highlighted by the dashed lines (see Fig. 3). This is associated with a reduction of frequency upon compression as a consequence of the first shell distance contraction, both for liquid Ni and Co.

For the analysis of the EXAFS data, pair distribution functions $g(r)$ derived from independent experiments (x-ray or neutron diffraction) or calculations such as molecular dynamics (MD) or Monte Carlo simulations can be used as starting models [48–50]. In particular, the $\chi(k)$ signal associated with the first neighbor shell can be expressed as

$$\chi(k) = \int_0^\infty 4\pi\rho r^2 g(r)\gamma^{(2)}(k,r)dr, \qquad (1)$$

where ρ is the number density and $\gamma^{(2)}(k,r)$ represents the dimensionless two-body contribution to the EXAFS signal associated with the single scattering by one atom at distance r from the photoabsorber.

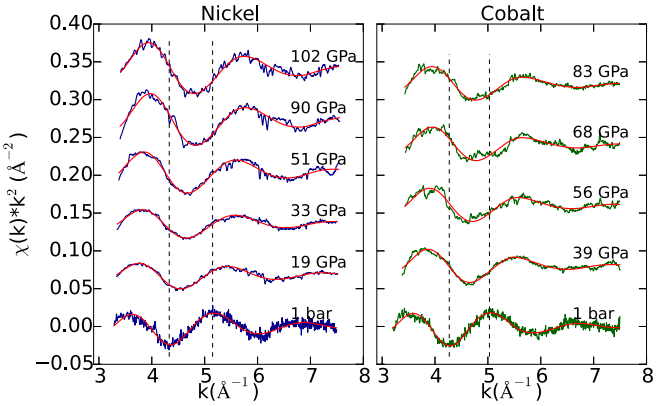

FIG. 3. Comparison between the Ni and Co K-edge experimental EXAFS spectra of liquid nickel and cobalt at different pressures along the melting curve (blue and green curves, for nickel and cobalt, respectively) and best-fit theoretical EXAFS signals (red curves). The data at ambient conditions are more noisy because they were acquired with a different experimental configuration (see Supplemental Material [41]). The dashed lines are a guide for the eyes and highlight the positions of the first minimum and second maximum of the oscillations for the signal at ambient pressure.

Model $g(r)$ for nickel under pressure were taken from previously published MD simulations [25,26] while for cobalt, *ab initio* quantum molecular dynamics (QMD) calculations were carried out that provided $g(r)$ covering different pressure-temperature conditions. QMD simulations were performed using the *ab initio* plane wave density functional theory code ABINIT [51–53] together with generalized gradient approximation [54] in the framework of the projected augmented wave (PAW) method [55,56]. The PAW data set for cobalt was generated using nine outer electrons ($3d^8 4s^1 4p^0$) and a cutoff radius, $r_c = 2.1a_B$ and a plane wave basis with an energy cutoff of 15 Ha. Two cubic simulation boxes including either 32 or 54 atoms were used. The electron temperature was controlled by the width of the Fermi-Dirac distribution and the ion temperature was controlled in the isokinetics ensemble where the velocity was rescaled at every time step to maintain the desired temperature. Configurations were propagated up to 8 ps using time steps of 2.5 fs. All MD calculations were performed with a $2 \times 2 \times 2$ mesh in the Monkorst-Pack scheme [57] for representation of the Brillouin zone.

The theoretical $g(r)$'s and their associated theoretical densities ρ provide the starting conditions for the EXAFS analysis. Due to experimental constraints linked to the very high pressure and temperature, the exploitable k-range of the EXAFS signal is limited between 3.0 and 7.5 Å^{-1} and does not allow performing a standard fitting procedure [58]. For each temperature and pressure, a model $g(r)$ was obtained by shifting the theoretical $g(r)$ previously obtained by MD simulation by different values. For each of the shifted $g(r)$ the theoretical $\chi(k)$ signals were calculated with Eq. (1) and compared with the experimental data as follows. Theoretical $\gamma^{(2)}$ signals were calculated with the GNXAS code [58,59] in the muffin-tin approximation using the Hedin-Lundqvist energy-dependent exchange and correlation potential model, which includes inelastic loss effects [59]. Least-squares fits of the EXAFS raw experimental data were performed to find the best-fit $g(r)$ position, and only one nonstructural parameter, namely, the amplitude reduction factor S_0^2 that accounts for the relaxation of passive electrons in the presence of a core hole, was varied during the analysis. The quality of the fits was determined by the goodness-of-fit parameter [58] and by careful inspection of the EXAFS residuals. Due to the well-known correlation between the first shell distance and E_0 (core ionization threshold energy) the latter parameter was kept fixed during the minimization procedure and was set at 5.0 and 8.0 eV above the first inflection point of the XAS spectra for nickel and cobalt, respectively. The presence of double electron excitations [60] was considered in the background modeling. Figure 3 shows the comparison between the EXAFS experimental spectra and the best-fit theoretical signals both for nickel and cobalt.

TABLE I. Pressure-temperature conditions for the analyzed nickel and cobalt spectra and the Ni-Ni and Co-Co first peak distance (R) resulting from the EXAFS analysis. The melting temperature at ambient pressure was not measured in this experiment.

Nickel			Cobalt		
P (GPa)	T (K)	R (Å)	P (GPa)	T (K)	R (Å)
10^{-4}	1728	2.39(5)	10^{-4}	1775	2.46(5)
11(1)	2220(340)	2.34(5)	10(1)	2020(100)	2.43(5)
19(2)	2420(190)	2.29(5)	31(3)	2930(210)	2.33(5)
28(3)	2750(250)	2.29(5)	39(4)	2660(260)	2.28(5)
33(3)	2990(300)	2.24(5)	41(4)	2730(280)	2.33(5)
45(5)	3120(270)	2.24(5)	56(6)	3590(260)	2.26(5)
51(5)	3350(360)	2.24(5)	68(7)	3660(300)	2.23(5)
90(9)	3200(380)	2.19(5)	83(8)	3620(460)	2.23(5)
102(10)	3600(290)	2.19(5)			

The agreement between the experimental and theoretical data is very good in all cases and the trend of the oscillations with pressure is nicely reproduced. The Ni-Ni and Co-Co first neighbor distances, defined as the maxima of the $g(r)$ first peak (Gaussian) obtained from the EXAFS data analysis, are reported in Table I. From the EXAFS experimental results a contraction of 0.20 Å for liquid nickel has been observed when the pressure is increased from ambient to 102 GPa along the melting curve. A similar result has been obtained for liquid cobalt where the Co-Co first neighbor distance undergoes a shortening of 0.23 Å when the pressure is increased from ambient to 83 GPa. Figure 4 shows the trend of the Ni-Ni and Co-Co first neighbor distances, as determined from the EXAFS analysis, as a function of pressure together with the theoretical results obtained by Cao *et al.* [25] and Lee and Lee [26] for nickel and by our QMD calculations for cobalt. The pressure and temperature conditions of both the theoretical calculations and experimental data are those shown in Fig. 2. As expected both liquid nickel and cobalt show a very similar compression along the melting curve. In the case of nickel, where both the experiment and the calculations by Cao *et al.* [25] are performed along the melting curve, the agreement between the experiment and the theory is very good. The calculations by Lee and Lee [26] and those obtained for cobalt in this work are instead performed along isotherms at 3000 and 5000 K, respectively. For cobalt even if

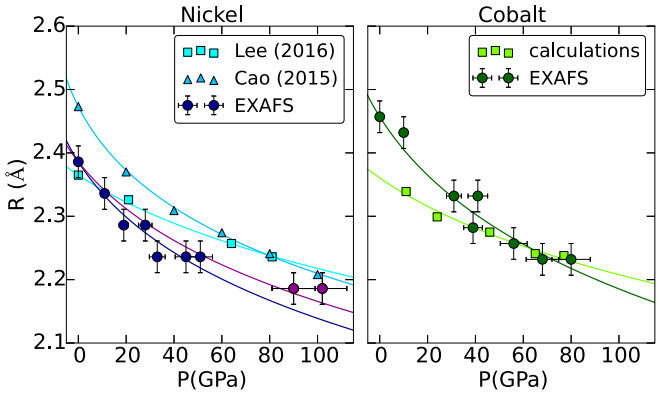

FIG. 4. Compression of the Ni-Ni and Co-Co first neighbor distances as a function of pressure obtained from the EXAFS analysis and compared with the theoretical results. The maxima of the $g(r)$ first peaks are plotted. The solid lines serve as a guide for the eye. Left panel: Ni-Ni first neighbor distances obtained from the EXAFS experimental data as a function of pressure (blue circles). The purple circles represent the Ni-Ni distances obtained for two samples contaminated with 7% of NiO, the compression trend of the Ni-Ni first distance is not strongly affected. The Ni-Ni first neighbor distances resulting from calculations by Cao *et al.* and Lee and Lee are shown as blue triangles and cyano squares, respectively [25,26]. Right panel: Co-Co first neighbor distances obtained from the EXAFS experimental data as a function of pressure (green circles) together with the values obtained from QMD molecular dynamics performed in this work (green squares).

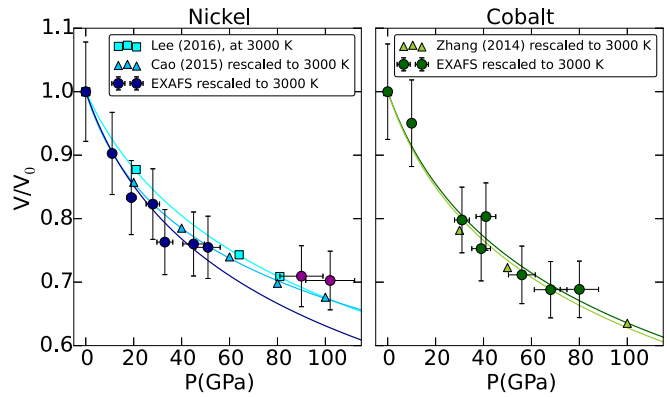

FIG. 5. Volume of liquid Ni and Co normalized to the volume at ambient pressure and rescaled to 3000 K. Left panel: Volume of Ni obtained from EXAFS experimental data as a function of pressure (blue and purple circles). Volumes by Lee and Lee already at 3000 K and volumes by Cao *et al.* rescaled to 3000 K are shown as light-blue triangles and cyano squares, respectively [25,26]. Right panel: Volume of Co obtained from EXAFS experimental data as a function of pressure (green circles) together with the values obtained by Zhang *et al.* with MD simulations performed with a Zhou's EAM potential (green triangles) [19]. The solid lines are obtained as Vinet fit of the data.

a direct comparison between the experimental and theoretical determinations is not possible, the compression of the Co-Co distance along the melting curve has a similar trend as that determined for nickel. The theoretical calculations carried out along the isotherm show a less steep distance contraction with increasing pressure. This is due to the opposite effect of temperature and pressure on the metal bond distance.

The obtained compression data were then exploited to give an evaluation of the specific volume. The specific volume was estimated from the maxima of the $g(r)$ first peak obtained with the EXAFS data analysis and then used to fit analytical equations of state (EoS) of liquid nickel and cobalt. This estimation is based on the assumption of $V/V_0 = R^3/R_0^3$, already proposed in the literature for metallic amorphous compounds [61] and for liquid Fe-5 wt % Ni-12 wt % S and Fe-5 wt % Ni-15 wt % Si [10]. Following the same procedure used for the two iron alloys [10], both experimental and theoretical data from the literature were corrected to a temperature of 3000 K and fit to a Vinet equation of state

$$P = 3K_{T,0}\, v^{-2/3}(1 - v^{1/3}) \exp\left[\tfrac{3}{2}(K' - 1)(1 - v^{1/3})\right], \quad (2)$$

where $v = \frac{V}{V_0}$, V is the volume under pressure, V_0 is the volume at ambient pressure, $K_{T,0}$ is the bulk modulus, and K' its first pressure derivative. The resulting volumes normalized to the volume at ambient pressure are presented in Fig. 5. By setting K' at 4 and the V_0 at the experimental value at ambient pressure, the Vinet fit of the experimental volumes gives a bulk modulus of 91(6) and 94(4) GPa at 3000 K for nickel and cobalt, respectively. These values are slightly higher than those extrapolated from the literature (Refs. [62,63]) for the solid, which are 88 and 87 GPa for nickel and cobalt, respectively. Details about the temperature correction [10] and the EoS fit [64,65] are provided in the Supplemental Material [41].

In the present work, EXAFS data were analyzed with the aim of measuring the first neighbor distance of high-pressure liquids along their melting curves. In particular, the Ni-Ni and Co-Co first neighbor distance contractions of liquid Ni and Co were experimentally determined at extreme conditions. Moreover, it was possible to give an estimation of the bulk modulus for the liquid Ni and Co at 3000 K by assuming $V/V_0 = R^3/R_0^3$ and performing a fit to the Vinet equation of state up to 51 and 83 GPa, respectively. This work provides a method suitable for the treatment of XAS data collected at extreme conditions of P and T, allowing the characterization of the liquid state of systems of geophysical and planetary relevance to be performed. This opens the possibility of characterizing, with XAS, the liquid core of several terrestrial planets such as Earth, Mars, Mercury, and Venus.

The authors acknowledge the European Synchrotron Radiation Facility (ESRF) for provision of synchrotron radiation within Projects HC-2554, HC-2593, HC-2882, and HC-2883. The authors are thankful to Jeroen Jacobs for technical support before the experiments and to Angelika Rosa and Olivier Mathon for practical help and helpful discussions.

[1] J. H. Eggert, G. Weck, P. Loubeyre, and M. Mezouar, Quantitative structure factor and density measurements of high-pressure fluids in diamond anvil cells by x-ray diffraction: Argon and water, Phys. Rev. B **65**, 174105 (2002).

[2] C. Sanloup, F. Guyot, P. Gillet, G. Fiquet, R. J. Hemley, M. Mezouar, and I. Martinez, Structural changes in liquid Fe at high pressures and high temperatures from synchrotron x-ray diffraction, Europhys. Lett. **52**, 151 (2000).

[3] G. Shen, V. B. Prakapenka, M. L. Rivers, and S. R. Sutton, Structure of Liquid Iron at Pressures up to 58 GPa, Phys. Rev. Lett. **92**, 185701 (2004).

[4] C. Sanloup, G. Fiquet, E. Gregoryanz, G. Morard, and M. Mezouar, Effect of Si on liquid Fe compressibility: Implications for sound velocity in core materials, Geophys. Res. Lett. **31**, 1 (2004).

[5] L. Koci, A. B. Belonoshko, and R. Ahuja, Molecular dynamics study of liquid iron under high pressure and high temperature, Phys. Rev. B **73**, 224113 (2006).

[6] X. Yu and R. A. Secco, Equation of state of liquid Fe-17 wt % Si to 12 GPa, High Press. Res. **28**, 19 (2008).

[7] H. Terasaki, K. Nishida, Y. Shibazaki, T. Sakamaki, A. Suzuki, E. Ohtani, and T. Kikegawa, Density measurement of Fe3C liquid using x-ray absorption image up to 10 GPa and effect of light elements on compressibility of liquid iron, J. Geophys. Res. **115**, 1 (2010).

[8] K. Nishida, E. Ohtani, S. Urakawa, A. Suzuki, T. Sakamaki, H. Terasaki, and Y. Katayama, Density measurement of liquid FeS at high pressures using synchrotron x-ray absorption x-ray, Am. Mineral. **96**, 864 (2011).

[9] C. Sanloup, W. V. Westrenen, R. Dasgupta, H. Maynard-Casely, and J. Perrillat, Compressibility change in iron-rich melt and implications for core formation models, Earth Planet. Sci. Lett. **306**, 118 (2011).

[10] G. Morard, J. Siebert, D. Andrault, N. Guignot, and G. Garbarino, The Earth's core composition from high pressure density measurements of liquid iron alloys, Earth Planet. Sci. Lett. **373**, 169 (2013).

[11] Y. Shimoyama, H. Terasaki, E. Ohtani, S. Urakawa, Y. Takubo, K. Nishida, A. Suzuki, and Y. Katayama, Density of Fe-3.5 wt % C liquid at high pressure and temperature and the effect of carbon on the density of the molten iron, Phys. Earth Planet. Inter. **224**, 77 (2013).

[12] J. Chen, T. Yu, S. Huang, J. Girard, and X. Liu, Compressibility of liquid FeS measured using x-ray radiograph imaging, Phys. Earth Planet. Inter. **228**, 294 (2014).

[13] R. Boehler, D. Santamaría-Pérez, D. Errandonea, and M. Mezouar, Melting, density, and anisotropy of iron at core conditions: New x-ray measurements to 150 GPa, J. Phys.: Conf. Ser. **121**, 022018 (2008).

[14] S. Anzellini, A. Dewaele, M. Mezouar, P. Loubeyre, and G. Morard, Melting of iron at Earth's inner core boundary based on fast x-ray diffraction, Science **340**, 464 (2013).

[15] G. Aquilanti, A. Trapananti, A. Karandikar, I. Kantor, C. Marini, O. Mathon, S. Pascarelli, and R. Boehler, Melting of iron determined by x-ray absorption spectroscopy to 100 GPa, Proc. Natl. Acad. Sci. USA **112**, 12042 (2015).

[16] G. Morard, S. Boccato, A. Rosa, S. Anzellini, F. Miozzi, L. Henry, G. Garbarino, M. Mezouar, M. Harmand, F. Guyot, E. Boulard, I. Kantor, T. Irifune, and R. Torchio, Solving controversies on the iron phase diagram under high pressure, Geophys. Res. Lett. **45**, 082 (2018).

[17] R. Sinmyo, K. Hirose, and Y. Ohishi, Melting curve of iron to 290 GPa determined in a resistance-heated diamond-anvil cell, Earth Planet. Sci. Lett. **510**, 45 (2019).

[18] O. T. Lord, I. G. Wood, D. P. Dobson, L. Vocadlo, W. Wang, A. R. Thomson, E. T. H. Wann, G. Morard, M. Mezouar, and M. J. Walter, The melting curve of Ni to 1 Mbar, Earth Planet. Sci. Lett. **408**, 226 (2014).

[19] W. J. Zhang, Y. F. Peng, and Z. L. Liu, Molecular dynamics study of melting curve, entropy of fusion and solid-liquid interfacial energy of cobalt under pressure, Physica B (Amsterdam) **440**, 33 (2014).

[20] S. Boccato, R. Torchio, I. Kantor, G. Morard, S. Anzellini, R. Giampaoli, R. Briggs, A. Smareglia, T. Irifune, and S. Pascarelli, The melting curve of nickel up to 100 GPa explored by XAS, J. Geophys. Res.: Solid Earth **122**, 9921 (2017).

[21] G. Morard, D. Andrault, D. Antonangeli, Y. Nakajima, A. L. Auzende, E. Boulard, S. Cervera, A. Clark, O. T. Lord, J. Siebert, V. Svitlyk, G. Garbarino, and M. Mezouar, Fe-FeO and Fe $-$ Fe_3C melting relations at Earth's core-mantle boundary conditions: Implications for a volatile-rich or oxygen-rich core, Earth Planet. Sci. Lett. **473**, 94 (2017).

[22] D. Antonangeli, L. R. Benedetti, D. L. Farber, Gerd Steinle-Neumann, A. L. Auzende, J. Badro, M. Hanfland, and M. Krisch, Anomalous pressure evolution of the axial ratio c/a in hcp cobalt: Interplay between structure, magnetism, and lattice dynamics, Appl. Phys. Lett. **92**, 111911 (2008).

[23] R. Torchio, A. Monza, F. Baudelet, S. Pascarelli, O. Mathon, E. Pugh, D. Antonangeli, and J. Paul Itié, Pressure-induced collapse of ferromagnetism in cobalt up to 120 GPa as seen via x-ray magnetic circular dichroism, Phys. Rev. B **84**, 060403(R) (2011).

[24] R. Torchio, Y. O. Kvashnin, S. Pascarelli, O. Mathon, C. Marini, L. Genovese, P. Bruno, G. Garbarino, A. Dewaele, F. Occelli, and P. Loubeyre, X-Ray Magnetic Circular Dichroism Measurements in Ni up to 200 GPa: Resistant Ferromagnetism, Phys. Rev. Lett. **107**, 237202 (2011).

[25] Q.-L. Cao, P.-P. Wang, D.-H. Huang, J.-S. Yang, M.-J. Wan, and F.-H. Wang, Properties of liquid nickel along melting lines under high pressure, Chin. Phys. Lett. **32**, 086201 (2015).

[26] B. Lee and G. W. Lee, A liquid-liquid transition can exist in monatomic transition metals with a positive melting slope, Sci. Rep. **6**, 35564 (2016).

[27] L. Yin, Research on first-principles calculations of the pressure-induced structure of liquid cobalt at high temperature, Nat. Sci. J. Harbin Norm. Univ. **5**, 42 (2011).

[28] Y. Waseda and S. Tamaki, The structures of 3d-transition metals in the liquid state, Philos. Mag. **32**, 273 (1975).

[29] M. W. Johnson, N. H. March, B. McCoy, S. K. Mitra, D. I. Page, and R. C. Perrin, Structure and effective pair interaction in liquid nickel, Philos. Mag. **33**, 203 (1976).

[30] F. J. Cherne, M. I. Baskes, and P. A. Deymier, Properties of liquid nickel: A critical comparison of EAM and MEAM calculations, Phys. Rev. B **65**, 024209 (2001).

[31] T. Schenk, D. Holland-Moritz, V. Simonet, R. Bellissent, and D. M. Herlach, Icosahedral Short-Range Order in Deeply Undercooled Metallic Melts, Phys. Rev. Lett. **89**, 075507 (2002).

[32] T. H. Kim and K. F. Kelton, Structural study of supercooled liquid transition metals, J. Chem. Phys. **126**, 054513 (2007).

[33] A. DiCicco, F. Iesari, S. DePanfilis, M. Celino, S. Giusepponi, and A. Filipponi, Local fivefold symmetry in liquid and undercooled Ni probed by x-ray absorption spectroscopy and computer simulations, Phys. Rev. B **89**, 060102(R) (2014).

[34] V. I. Lad'yanov, A. L. Bel'tyukov, K. G. Tronin, and L. V. Kamaeva, Structural transition in liquid cobalt, JETP Lett. **72**, 301 (2000).

[35] A. F. Crawley, Densities of liquid metals and alloys, Int. Metall. Rev. **19**, 32 (1974).

[36] S. Pascarelli, O. Mathon, T. Mairs, I. Kantor, G. Agostini, C. Strohm, S. Pasternak, F. Perrin, G. Berruyer, P. Chappelet, C. Clavel, and M. C. Dominguez, The time-resolved and extreme-conditions XAS (TEXAS) facility at the European synchrotron radiation facility: The energy-dispersive x-ray absorption spectroscopy beamline ID24, J. Synchrotron Radiat. **23**, 353 (2016).

[37] T. Irifune, A. Kurio, S. Sakamoto, T. Inoue, and H. Sumiya, Ultrahard polycrystalline diamond from graphite, Nature **421**, 599 (2003).

[38] H. K. Mao, J. Xu, and P. M. Bell, Calibration of the ruby pressure gauge to 800 kbar under quasi-hydrostatic conditions, J. Geophys. Res. **91**, 4673 (1986).

[39] L. Benedetti and P. Loubeyre, Temperature gradients, wavelength-dependent emissivity, and accuracy of high and very-high temperatures measured in the laser-heated diamond cell, High Press. Res. **24**, 423 (2004).

[40] R. Giampaoli, I. Kantor, M. Mezouar, S. Boccato, A. D. Rosa, R. Torchio, G. Garbarino, O. Mathon, and S. Pascarelli, Measurement of temperature in the laser heated diamond anvil cell: Comparison between reflective and refractive optics, High Press. Res. **38**, 250 (2018).

[41] See Supplemental Material at http://link.aps.org/supplemental/10.1103/PhysRevB.100.180101 for more details on the experimental procedures and the EoS fit.

[42] S. Boccato, Local structure of liquid 3d metals under extreme conditions of pressure and temperature, Ph.D. thesis, Université Grenoble Alpes, 2017.

[43] R. Torchio, S. Boccato, V. Cerantola, G. Morard, T. Irifune, and I. Kantor, Probing the local, electronic and magnetic structure of matter under extreme conditions of temperature and pressure, High Press. Res. **36**, 293 (2016).

[44] I. Kantor, C. Marini, O. Mathon, and S. Pascarelli, A laser heating facility for energy-dispersive x-ray absorption spectroscopy, Rev. Sci. Instrum. **89**, 013111 (2018).

[45] I. Kantor, J.-C. Labiche, E. Collet, L. Siron, J.-J. Thevenin, C. Ponchut, J. Borrel, T. Mairs, C. Marini, C. Strohm, O. Mathon, and S. Pascarelli, A new detector for sub-millisecond EXAFS spectroscopy at the European synchrotron radiation facility, J. Synchrotron Radiat. **21**, 1240 (2014).

[46] P. Lazor, Phase diagrams, elasticity and thermodynamics of Ni, Co and Fe under high pressure, Ph.D. thesis, Faculty of Science and Technology, 1994.

[47] A. D. Cicco and A. Trapananti, Study of local icosahedral ordering in liquid and undercooled liquid copper, J. Non-Cryst. Solids **353**, 3671 (2007).

[48] A. Filipponi, EXAFS for liquids, J. Phys.: Condens. Matter **13**, R23 (2001).

[49] V. T. Pham, I. Tavernelli, C. J. Milne, R. M. van der Veen, P. D'Angelo, Ch. Bressler, and M. Chergui, The solvent shell structure of aqueous iodide: X-ray absorption spectroscopy and classical, hybrid QM/MM and full quantum molecular dynamics simulations, Chem. Phys. **371**, 24 (2010).

[50] V. Migliorati, F. Sessa, G. Aquilanti, and P. D'Angelo, Unraveling halide hydration: A high dilution approach, J. Chem. Phys. **141**, 044509 (2014).

[51] The ABINIT code is a common project of the Université Catholique de Louvain, Corning Inc., the Commissariat à l'Energie Atomique, the Université de Liège, Mitsubishi Chemical Corp., and other contributors, http://www.abinit.org.

[52] X. Gonze, B. Amadon, P.-M. Anglade, J.-M. Beuken, F. Bottin, P. Boulanger, F. Bruneval, D. Caliste, R. Caracas, M. Côté, T. Deutsch, L. Genovese, Ph. Ghosez, M. Giantomassi, S. Goedecker, D. R. Hamann, P. Hermet, F. Jollet, G. Jomard, S. Leroux, M. Mancini, S. Mazevet, M. J. T. Oliveira, G. Onida, Y. Pouillon, T. Rangel, G.-M. Rignanese, D. Sangalli, R. Shaltaf, M. Torrent, M. J. Verstraete, G. Zerah, and J. W. Zwanziger, ABINIT: First-principles approach to material and nanosystem properties, Comput. Phys. Commun. **180**, 2582 (2009).

[53] F. Bottin, S. Leroux, A. Knyazev, and G. Zerah, Large-scale ab initio calculations based on three levels of parallelization, Comput. Mater. Sci. **42**, 329 (2008).

[54] J. P. Perdew, K. Burke, and M. Ernzerhof, Generalized Gradient Approximation Made Simple, Phys. Rev. Lett. **77**, 3865 (1996).

[55] P. E. Blöchl, Generalized separable potentials for electronic-structure calculations, Phys. Rev. B **41**, 5414 (1990).

[56] M. Torrent, F. Jollet, F. Bottin, and G. Zerah, Implementation of the projector augmented-wave method in the ABINIT code: Application to the study of iron under pressure, Comput. Mater. Sci. **42**, 337 (2008).

[57] H. J. Monkhorst and J. D. Pack, Special points for Brillouin-zone integrations, Phys. Rev. B **13**, 5188 (1976).

[58] A. Filipponi and A. DiCicco, X-ray-absorption spectroscopy and *n*-body distribution functions in condensed matter. II. Data analysis and applications, Phys. Rev. B **52**, 15135 (1995).

[59] A. Filipponi, A. DiCicco, and C. R. Natoli, X-ray-absorption spectroscopy and *n*-body distribution functions in condensed matter. I. Theory, Phys. Rev. B **52**, 15122 (1995).

[60] A. Filipponi, Double-electron excitation effects above inner shell x-ray absorption edges, Physica B: Condensed Matter **208–209**, 29 (1995).

[61] J. Z. Jiang, W. Roseker, M. Sikorski, Q. P. Cao, and F. Xu, Pressure effect of glass transition temperature in $Zr_{46.8}Ti_{8.2}Cu_{7.5}Ni_{10}Be_{27.5}$ bulk metallic glass, Appl. Phys. Lett. **84**, 1871 (2004).

[62] Z.-Y. Zeng, C.-E. Hu, L. C. Cai, and F.-Q. Jing, *Ab initio* study of lattice dynamics and thermal equation of state of Ni, Phys. B (Amsterdam, Neth.) **407**, 330 (2012).

[63] M. M. Armentrout and A. Kavner, A new high pressure and temperature equation of state of fcc cobalt, J. Appl. Phys. **118**, 194904 (2015).

[64] R. J. Angel, J. Gonzalez-Platas, and M. Alvaro, EosFit7c and a Fortran module (library) for equation of state calculations, Z. Kristallogr. **229**, 405 (2014).

[65] J. Gonzalez-Platas, M. Alvaro, F. Nestola, and R. Angel, EosFit7-GUI: A new graphical user interface for equation of state calculations, analyses and teaching, J. Appl. Crystallogr. **49**, 1377 (2016).